Laser Engineered Slippery Liquid Infused Porous Surfaces (SLIPS) on 3D Printed Metal Alloys

Mohammad Mohammadzadeh Sanandaji[a], Hao Fu[b], and Hongtao Ding[a,*]

[a] Department of Mechanical Engineering, University of Iowa, Iowa City, IA 52242, USA
[b] Han's Laser Corp., San Jose, CA 95131, USA

Abstract

Laser powder bed fusion (L-PBF) inherently produces metallic surfaces with high roughness and porosity, which limits their direct use in applications requiring low interfacial adhesion and controlled liquid mobility. In this work, a scalable strategy is presented for fabricating slippery liquid-infused porous surfaces (SLIPS) directly on as-printed L-PBF Ti6Al4V and AlSi10Mg alloys. Laser surface texturing using nanosecond and picosecond pulsed lasers was employed to restructure the irregular AM surface topography into well-defined microchannel networks that act as capillary reservoirs for lubricant retention. Following fluorosilane functionalization and silicone oil infusion, the resulting SLIPS exhibited static water contact angles exceeding 105° and sliding angles below 10°. Compared with untreated and laser-textured substrates, ice adhesion strength was reduced from approximately 370–460 kPa to ~65 kPa for Ti6Al4V and ~90 kPa for AlSi10Mg. The fabricated SLIPS maintained stable performance during repeated icing and deicing cycles and after mechanical abrasion, thermal exposure, and ultraviolet irradiation, indicating good durability and self-replenishing behavior. Overall, this work demonstrates a direct and versatile route for integrating SLIPS functionality with additively manufactured metal alloys, bridging L-PBF and laser surface engineering to enable durable anti-icing surfaces for aerospace, marine, and energy applications.

Keywords:

Slippery liquid-infused porous surface; Laser processing; Laser powder bed fusion

∗ Corresponding author
E-mail: hongtao-ding@uiowa.edu

1. Introduction

Laser-based metal additive manufacturing (AM), particularly laser powder bed fusion (L-PBF) and directed energy deposition (DED) has enabled the production of metal components with complex geometries and tailored microstructures that are difficult to achieve using conventional methods. These 3D-printed metals are now widely deployed across aerospace [1], marine [2], and energy [3], where they operate under demanding environmental conditions involving icing, corrosion, and biofouling. In such settings, ice accumulation on aircraft components[4], offshore platforms [5], and wind turbine blades can degrade performance, increase drag, and compromise safety.

Traditional de-icing strategies, such as thermal heating, mechanical removal, or chemical coatings[6,7] are often energy intensive, maintenance heavy, or environmentally harmful. These limitations have prompted growing interest in passive surface engineering approaches, notably superhydrophobic surfaces (SHS) and slippery liquid-infused porous surfaces (SLIPS), which aim to provide low adhesion, self-cleaning, and ice-phobic properties with minimal energy input.

SHS, inspired by the lotus leaf, rely on hierarchical roughness and low surface energy to trap air pockets beneath water droplets, reducing ice adhesion and delaying freezing [8–10]. Huang et al. demonstrated SHS on 3D-printed AlSi10Mg and Ti6Al4V alloys using laser texturing and chemical treatment, achieving both lotus leaf and rose petal wetting effects [11] However, SHS coatings often lose functionality under mechanical wear or prolonged exposure, as the entrapped air layer collapses when wetted or contaminated [12,13].

SLIPS, inspired by the Nepenthes pitcher plant, offer a more robust solution. By infusing lubricants into textured surfaces with low surface energy, SLIPS form a stable, self-healing liquid interface that repels water and contaminants [14]. Unlike SHS, SLIPS maintain performance under dynamic conditions and have shown strong resistance to icing, corrosion, and biofouling [15,16]. For example, Zhang et al. used femtosecond laser processing to create microporous SLIPS on stainless steel, achieving excellent ice resistance and durability [17]. Sakuraba et al. applied a similar method to anodized aluminum, demonstrating corrosion protection and self-healing behavior without organic primers [18]. Deng et al. further validated SLIPS effectiveness in marine environments, showing resistance to microbial and macrofouling [19].

Despite these advances, the integration of SLIPS with as-printed additively manufactured metals remains a critical gap in current research. Most existing studies utilize substrates that have been mechanically polished, ground, or anodized, resulting in smooth baseline surfaces with roughness typically below 2 μm. In contrast, laser powder bed fusion (L-PBF) produces surfaces with inherently high roughness. For example, as-printed L-PBF Ti6Al4V surfaces typically exhibit S_a values in the range of ~8–12 μm, while AlSi10Mg surfaces often display even higher roughness, commonly ~20–25 μm, prior to any surface modification or post-processing [11,20]. This extreme topography typically viewed as a defect poses a significant challenge for lubricant stability, as irregular asperities often lead to droplet pinning and rapid lubricant depletion.

Laser surface texturing offers a scalable, mask-free means of overcoming these challenges by imposing well-defined microchannel architectures onto the native AM topography. By transforming irregular, non-directional surface features into continuous, capillary-connected networks, laser texturing enables improved lubricant confinement and enhanced interfacial stability. While previous studies have utilized laser-induced microstructures to tailor wetting on

conventional metals, extending this approach to the extreme roughness of as-printed L-PBF alloys provides a unique opportunity to leverage inherent porosity as a functional lubricant reservoir [21,22].

In this study, SLIPS are integrated onto as-printed Ti6Al4V and AlSi10Mg surfaces without any prerequisite substrate smoothing or chemical etching. We systematically compare the effects of nanosecond and picosecond laser texturing to reveal how microchannel depth and continuity influence lubricant retention, durability, and anti-icing performance. Furthermore, the approach is applied to curved, three-dimensional AM components to demonstrate scalability to realistic geometries. Ultimately, this work bridges the gap between metal additive manufacturing and laser surface engineering by addressing the key durability and manufacturability challenges of SLIPS for AM components in extreme environments.

2. Method

The overall fabrication workflow is illustrated in Fig. 1 and consists of three main steps: (1) laser surface texturing and patterning, (2) fluorosilane functionalization to create a superhydrophobic surface, and (3) silicone-oil infusion to form slippery liquid-infused porous surfaces (SLIPS).

Laser processing is used at two length scales. Laser patterning defines the regions of the surface to be modified, enabling application of the process to both flat and three-dimensional additively manufactured parts. Within the patterned regions, laser texturing produces capillary-connected microchannels that form the textured zone, which serves as the primary functional area of the surface. After fluorosilane treatment, the superhydrophobic effect is strongest in the textured zone due to the oxide-rich surface formed during laser texturing, which enhances chemical bonding with the fluorosilane molecules [23]. Subsequent silicone-oil infusion converts these same regions into SLIPS, where the interconnected microchannels provide effective lubricant retention. As a result, SLIPS performance is also strongest within the laser-textured zones.

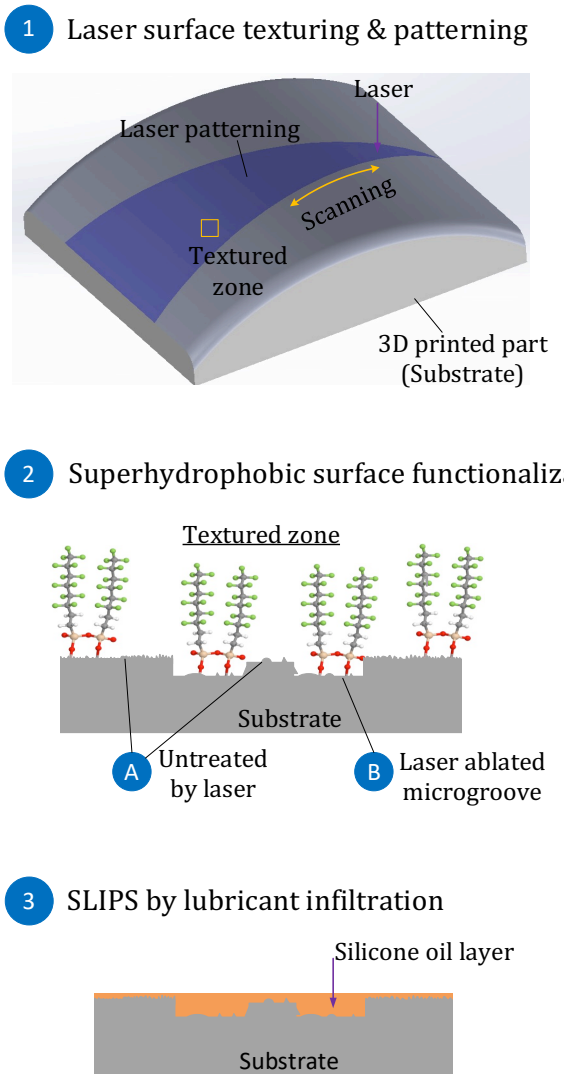

Fig. 1. Overview of the fabrication process for SLIPS on 3D-printed metal parts

In this work, Ti6Al4V and AlSi10Mg alloys were selected as base materials due to their widespread use in additive manufacturing and relevance to engineering applications. Samples were fabricated using laser powder bed fusion (L-PBF), a technique known for its cost effectiveness and consistent build quality. All samples were printed with a horizontal build orientation, such that the plane of the disk was parallel to the printing plane (0° inclination). Two flat sample geometries were used: 13 × 13 mm and 15 × 100 mm for experiments.

To demonstrate the scalability of the SLIPS process, additional three-dimensional and curved AlSi10Mg components of different sizes were also fabricated. These parts were printed using the same L-PBF parameters and build orientation as the flat coupons to ensure comparable microstructure and surface conditions prior to laser texturing. All samples were produced at the Quad City Manufacturing Lab using an EOS M270 system.

2.1 Laser Processing

Laser surface texturing was employed to generate controlled micro- and nanoscale features on the L-PBF Ti6Al4V and AlSi10Mg surfaces. Two laser systems were used for surface texturing. Nanosecond laser processing was carried out using a pulsed Nd:YAG laser (Spectra-Physics Quanta-Ray Lab-150, 1064 nm, 10 Hz) focused with a 255 mm focal-length lens to produce 120 ns pulses. Picosecond laser texturing was performed using a pulsed laser system (Han's Laser Co., 1064 nm), as shown in Fig. 2a. For nanosecond processing, a single pass scanning strategy with a 50% overlap ratio and fixed parameters was used, producing microchannels with widths and depths on the order of several hundred micrometers due to the high energy delivered per pulse. In contrast, the picosecond laser, operating at a much higher repetition rate, was applied using both single-pass and multi-pass scanning strategies with 50 % overlap ratio. While single-pass scans produced shallow surface features, multi-pass scans were required to increase channel depth and continuity. The complete processing parameters for both laser systems are summarized in Table 1.

In this work, a simple stripe-based patterning design combined with a unidirectional grooved microchannel texture was selected as a representative example to demonstrate controlled and repeatable laser processing on L-PBF metal surfaces (Fig. 2b). This specific pattern and texture are not intended to be limiting. Depending on the intended application and functional requirements of a component, alternative patterning layouts such as grid or localized regions and surface textures can be readily achieved by adjusting the laser scan path and processing parameters.

In this context, patterning refers to part-level laser processing that defines where surface modification is applied on the component, while texturing refers to the micro-scale laser ablation that generates the grooved microchannel structures within the patterned regions. A representative laser scanning layout is shown, which indicates laser-modified regions on the ridge areas (A) and within the microchannel interiors (B). These laser-induced microchannels form the capillary architecture required for lubricant retention and are produced uniformly on both flat and curved L-PBF components, as illustrated in Fig. 2c.

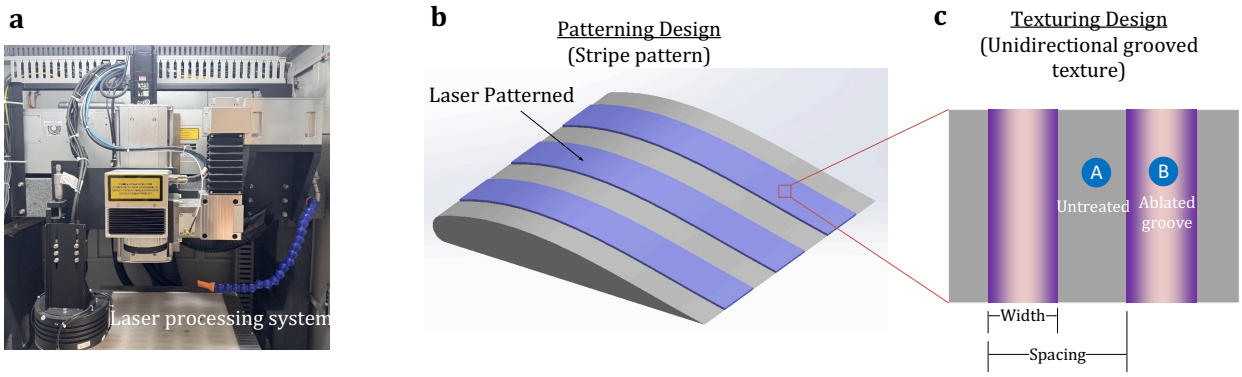

Fig. 2: Laser surface texturing setup and processing strategy for L-PBF metal parts: (a) picosecond laser processing system (Han's Laser Co.); (b) Schematic of laser-textured curved component demonstrating uniform patterning on a non-planar surface; (c) schematic of a laser-textured zone showing untreated and ablated area.

Table 1. Laser parameters for surface processing.

Laser type	*P (W)*	*D (μm)*	*V (mm/s)*	f_{rep} *(Hz)*	*Line spacing (μm)*	*F (J/cm²)*
NS laser	0.95	100	1.2	10	250	1.2×10^3
PS laser	15	40	100	50000	100	24

2.2 Fabrication of SHS and SLIPS

After laser texturing, samples were ultrasonically cleaned sequentially in acetone for 3 min, followed by ethyl alcohol for 3 min, and finally distilled water for 3 min. After cleaning, the samples were dried using compressed air at room temperature prior to surface functionalization. Then the samples were chemically modified to reduce surface energy and prepare them for lubricant infusion. The substrates were first functionalized with fluorosilane groups by immersion in a 2 wt% solution of 1H,1H,2H,2H-perfluorodecyltriethoxysilane (FAS) in ethanol for 3 hours at room temperature. The samples were then heat-treated at 120 °C for 30 minutes to promote covalent bonding of the silane molecules and form a stable fluorinated layer, resulting in superhydrophobic surfaces.

SLIPS were fabricated by immersing the superhydrophobic samples in silicone oil in a sealed container for 1 h, allowing the lubricant to infiltrate the laser-induced microstructures via capillary action. The silicone oil had a surface tension of approximately 21 mN/m, a viscosity of 20 mPa·s (at 25 °C), a density of 0.93 g/mL (at 25 °C), and thermal stability over the range of −50 °C to 200 °C. After infusion, excess lubricant was removed by tilting the samples at a 50° angle for 30 minutes, leaving a uniform and stable lubricant layer on the surface.

2.3 Characterization

The wettability and surface characteristics of the samples were evaluated through both static and dynamic water contact angle measurements. Static contact angles were measured using a Rame-Hart Model 100 goniometer equipped with a high-resolution CMOS camera (6–60× magnification, Thorlabs). Dynamic droplet behavior was assessed using tilt-angle tests, in which a 10 μL water droplet was placed on the surface and the inclination angle required for it to roll off was recorded. Surface topography was analyzed using a confocal laser scanning microscope (Keyence VK-X1000) to obtain three-dimensional surface profiles and quantify roughness parameters. Additional morphological characterization was performed using a Hitachi S-3400N scanning electron microscope (SEM), and surface chemistry was examined via energy-dispersive X-ray spectroscopy (EDS).

3. Results and Discussion

3.1 Surface morphology and chemistry

Photographs of the laser-processed flat and curved AlSi10Mg and Ti6Al4V samples are shown in Fig. 3, along with representative SEM image of the processed AlSi10Mg surface. The SEM image reveal that the laser-induced microgrooves are composed of interconnected cavities that form continuous microchannels. The ridge and valley regions of these microchannels are decorated with hierarchical nano- and micro-scale features. These fine surface structures are primarily attributed to material melting and resolidification accompanied by melt expulsion during laser ablation.

The surface topographic characteristics of the SLIPS samples were first analyzed using confocal microscopy. Fig 4 shows the three-dimensional surface topographies of L-PBF Ti6Al4V and AlSi10Mg samples in their as-printed, laser-textured, and SLIPS-treated states. The as-printed surfaces exhibit the characteristic irregular morphology associated with laser powder bed fusion, including partially fused particles, melt pool traces, and shallow surface depressions. The corresponding areal roughness values are S_a = 7.4 μm for Ti6Al4V and S_a = 25.3 μm for AlSi10Mg, reflecting moderately rough surfaces dominated by random, non-directional features.

After laser texturing, both alloys display well-defined, parallel microchannels aligned with the laser scanning direction. These microchannels substantially increase the developed surface area and introduce continuous ridge–valley structures across the surface. As a result, the areal roughness increases markedly to S_a = 122.4 μm for Ti6Al4V and S_a = 115.4 μm for AlSi10Mg, confirming the formation of pronounced microchannel morphologies. The regular channel network provides continuous grooves capable of storing and redistributing lubricant across the surface.

Notably, the laser-textured Ti6Al4V surfaces exhibit more uniform and deeper microchannels compared with AlSi10Mg. This difference is attributed to the higher melting point and more stable laser material interaction of Ti6Al4V, which promotes cleaner ablation and reduced recast formation. The resulting microchannel architecture yields a more interconnected groove network, which is favorable for capillary-driven lubricant transport.

Following silicone oil infusion, the SLIPS treated samples show a clear smoothing of the surface topography. The areal roughness decreases to S_a = 35.4 μm for Ti6Al4V and S_a = 48.2 μm for AlSi10Mg. This reduction arises from lubricant filling of the microchannel valleys and partial coverage of surface asperities, forming a conformal liquid layer that attenuates sharp height variations. The more uniform height distribution observed in the SLIPS topography maps indicates effective infiltration of the lubricant and the formation of a continuous liquid film across the laser-textured surfaces.

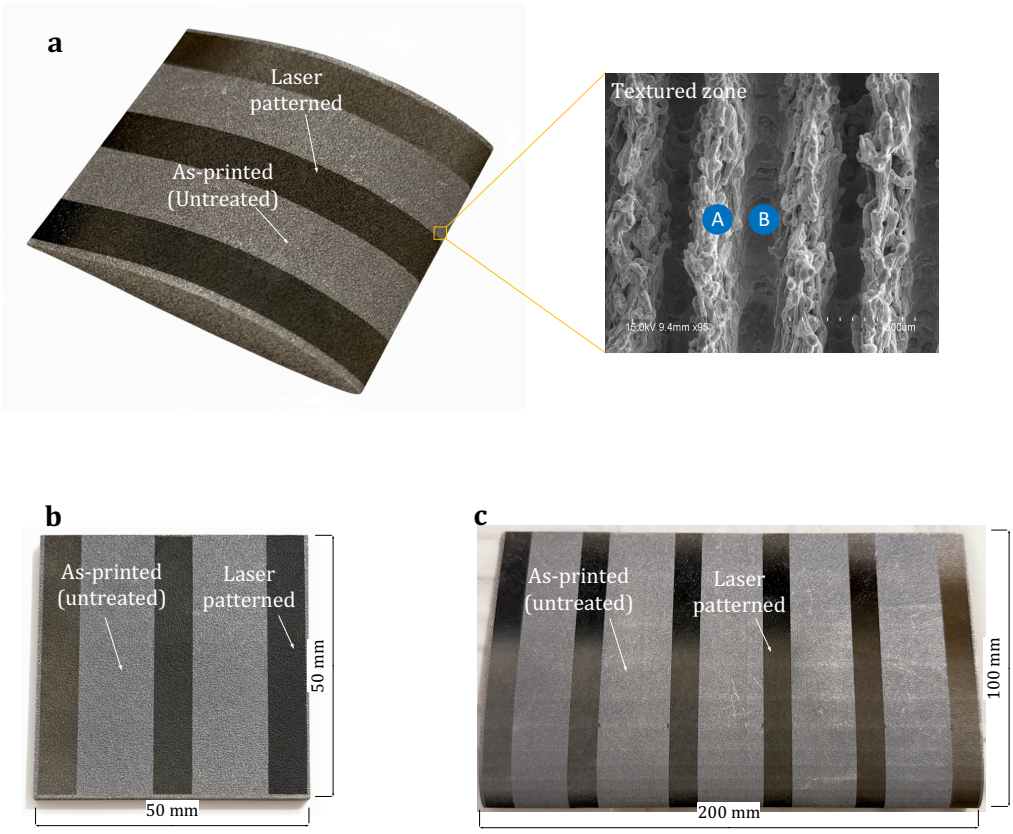

Fig. 3. Laser-textured L-PBF metal samples and surface morphology: (a) laser-textured curved AlSi10Mg component demonstrating uniform patterning on a non-planar surface with SEM image of a laser-textured surface; (b) flat Ti6Al4V coupon showing alternating laser-textured and untextured regions; (c) laser-textured curved AlSi10Mg component with a different geometry.

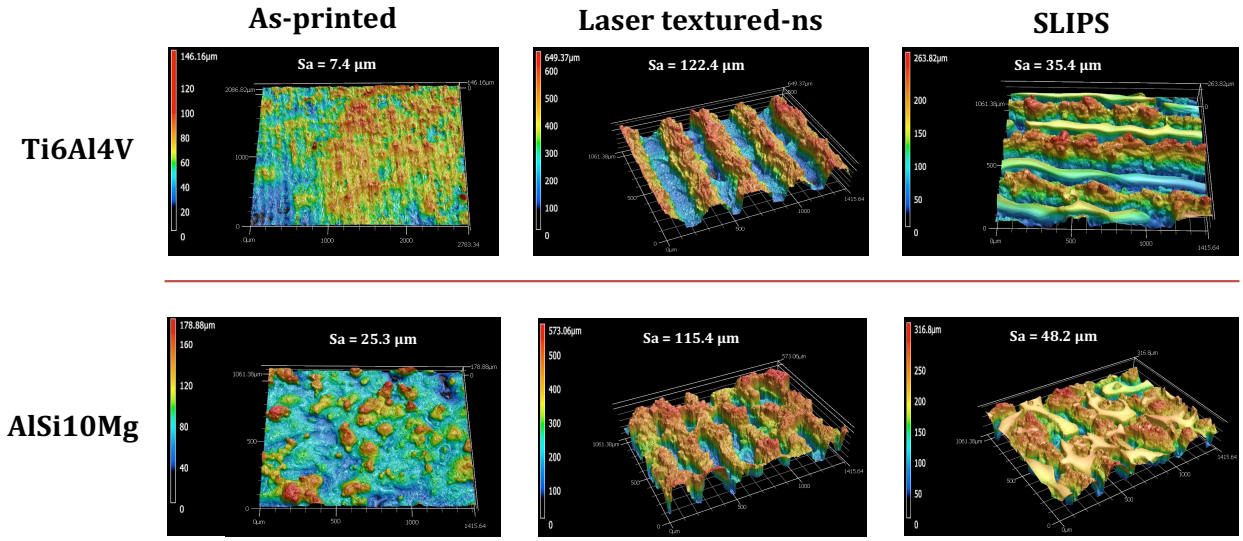

Fig. 4. Surface topography of L-PBF metal parts at different modification stages, as-printed, laser textured and SLIPS.

The effect of picosecond laser texturing on surface morphology was further examined by varying the number of laser passes for both AlSi10Mg and Ti6Al4V, as shown in Figs. 5 and 6 respectively. For both alloys, increasing the number of picosecond laser passes from 1 to 20 resulted in only modest changes in the areal roughness of the laser-textured surfaces, with Sa values remaining on the order of several tens of micrometers. This behavior indicates that picosecond laser processing produces relatively shallow microchannels that are superimposed onto the original L-PBF surface morphology.

The characteristic depth of the microchannels formed by picosecond laser texturing was approximately 20 µm, which is comparable to the inherent roughness of the as-printed surfaces. As a result, the picosecond laser does not fundamentally replace the L-PBF surface features but instead modifies the near-surface topography by introducing shallow channels across existing asperities. After lubricant infusion, the corresponding SLIPS-treated surfaces exhibit consistently lower Sa values, reflecting surface smoothing due to lubricant filling of shallow features and the formation of a conformal liquid layer.

In contrast, nanosecond laser texturing produces significantly deeper microchannels, with characteristic depths of approximately 350 µm, which are more than an order of magnitude larger than those produced by the picosecond laser. These deeper channels provide substantially larger lubricant reservoirs and more effective capillary confinement. Consequently, SLIPS fabricated on picosecond-laser-textured surfaces show reduced lubricant retention and durability compared with those fabricated using nanosecond laser texturing, consistent with the limited storage capacity associated with shallow microchannel architectures.

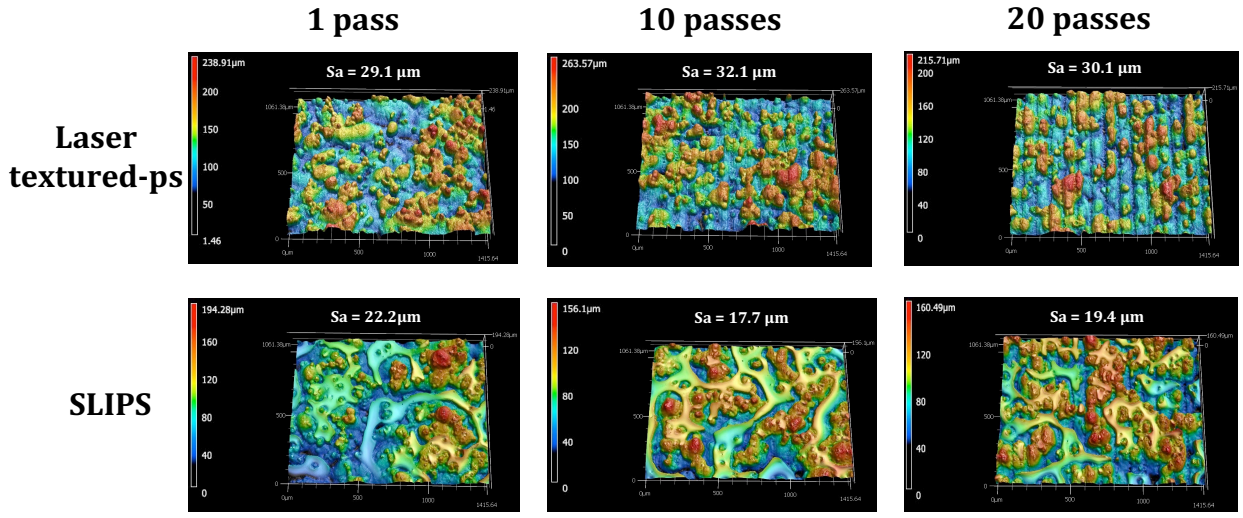

Fig. 5. Picosecond laser textured AlSi10Mg surfaces: three-dimensional confocal surface profiles of laser-textured and SLIPS-treated samples for different numbers of laser passes (1, 10, and 20), with corresponding areal roughness (S_a) values.

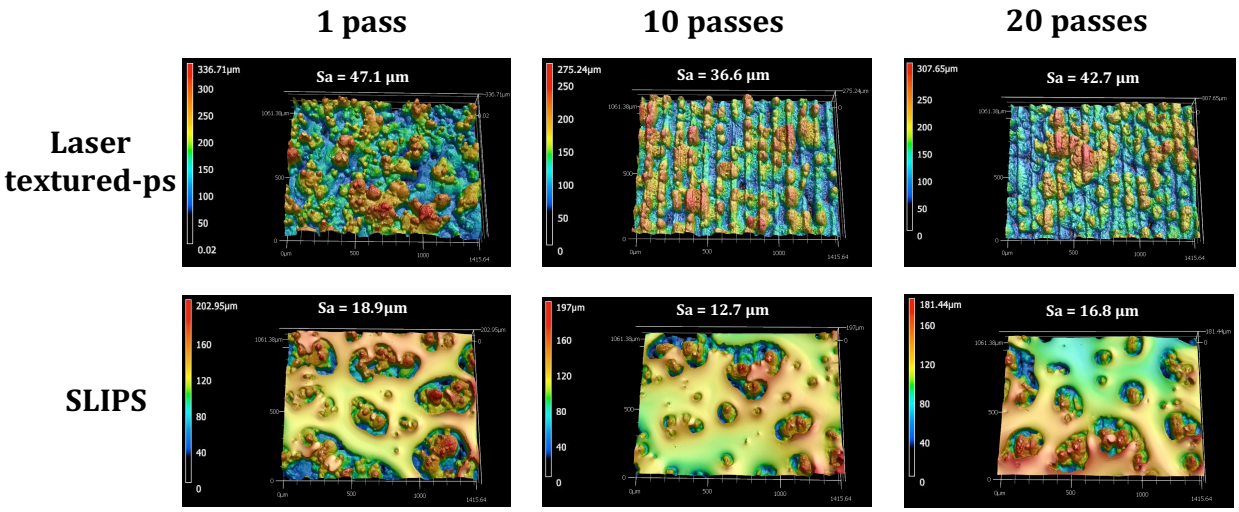

Fig. 6. Picosecond laser textured Ti6Al4V surfaces: three-dimensional confocal surface profiles of laser-textured and SLIPS-treated samples for different numbers of laser passes (1, 10, and 20), with corresponding areal roughness (S_a) values.

To evaluate the chemical distribution and uniformity of the SLIPS coating on nanosecond-laser-textured surfaces, SEM imaging combined with energy-dispersive X-ray spectroscopy (EDS) was performed, as shown in Fig. 7. The SEM images reveal a well-defined microchannel architecture on both Ti6Al4V and AlSi10Mg surfaces after lubricant infusion, with distinct ridge regions (A) and microchannel interiors (B) resulting from laser ablation.

For Ti6Al4V (Fig. 7a), the reported elemental maps show that the Si, O, and C signals associated with the infused silicone oil are predominantly concentrated within the microchannel interiors (B), following the laser-textured channel pattern. In contrast, the Ti signal is primarily localized on the ridge regions (A), where the lubricant layer is thinner, and the underlying substrate is more exposed. This spatial separation between lubricant-rich channels and Ti-rich ridges indicates preferential lubricant retention within the microchannels and confirms effective confinement of the liquid phase.

A similar elemental distribution is observed for AlSi10Mg (Fig. 7b). The Si, O, and C maps again correspond closely to the microchannel interiors (B), while the Al signal is more prominent on the ridge regions (A). Compared with Ti6Al4V, the lubricant distribution on AlSi10Mg appears less uniform, which is consistent with the more irregular microchannel morphology observed in the SEM images and the confocal topography measurements.

Overall, the combined SEM and EDS results confirm that silicone oil preferentially occupies the laser-induced microchannels, forming a continuous liquid-infused network across the textured surfaces. The more uniform confinement of the lubricant within the Ti6Al4V microchannels correlates with the enhanced lubricant retention and durability observed for Ti-based SLIPS surfaces under mechanical and environmental testing.

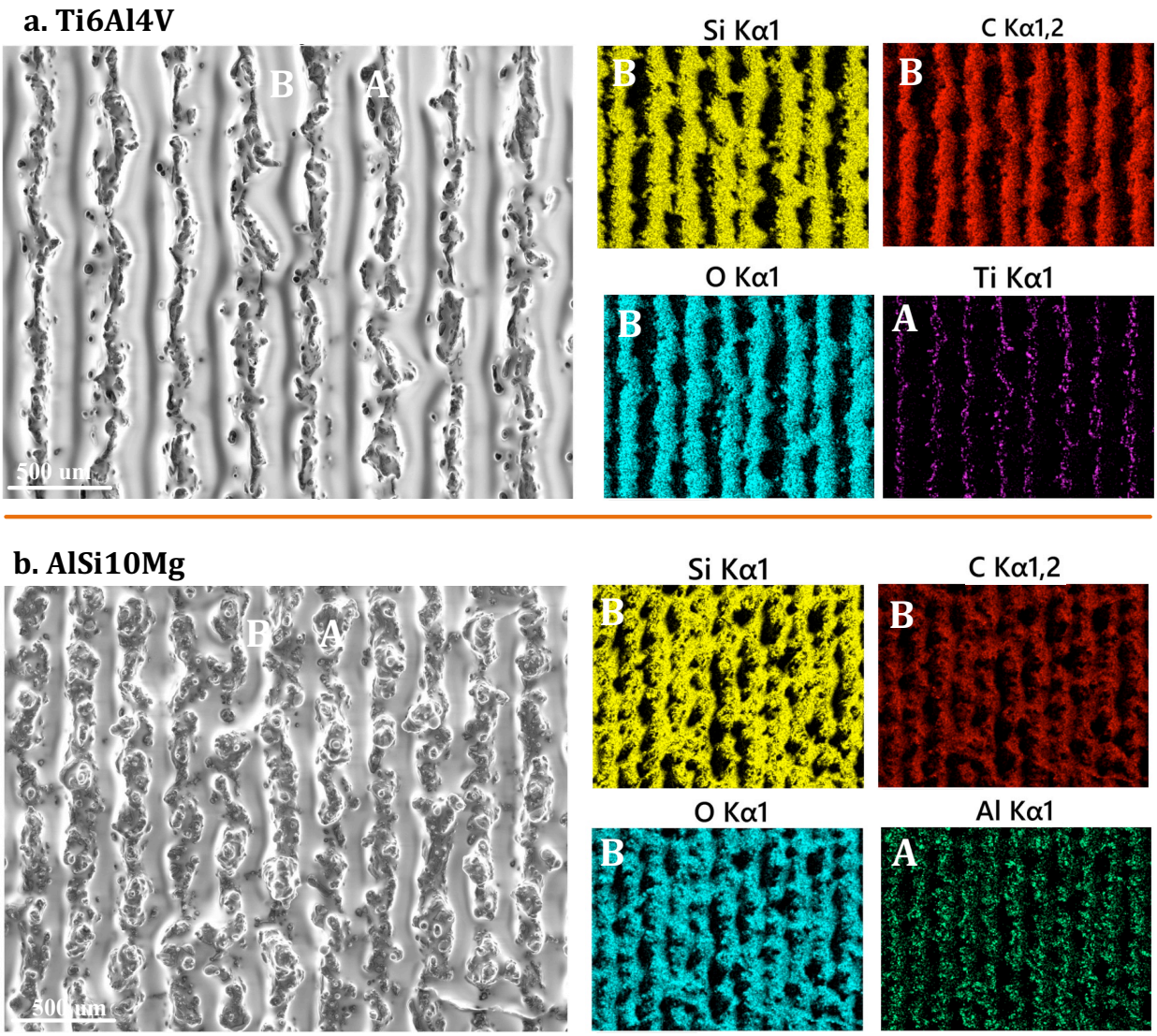

Fig. 7. SEM images and corresponding EDS elemental maps of SLIPS-coated surfaces fabricated by nanosecond laser texturing: (a) Ti6Al4V and (b) AlSi10Mg after lubricant infusion.

3.2 Wettability of SLIPS

The wetting behavior of the fabricated surfaces was evaluated by measuring the static contact angle (θ_w) and sliding angle (θ_s) for Ti6Al4V and AlSi10Mg samples. Fig. 8 summarizes the wettability evolution for the as-printed surfaces and SLIPS fabricated using nanosecond (SLIPS–ns) and picosecond (SLIPS–ps) laser texturing.

The as-printed samples exhibited moderate wettability, with static contact angles of around 42° for Ti6Al4V and 83° for AlSi10Mg (Fig. 8b). The corresponding sliding angles were relatively high (~80°; Fig. 8a), indicating strong droplet pinning caused by the rough surface morphology and the presence of native oxide layers typical of L-PBF metals.

After SLIPS fabrication using nanosecond laser texturing, a pronounced reduction in sliding angle was observed for both alloys, with θ_s decreasing to below 10°. At the same time, the static contact angles increased to approximately 115° for Ti6Al4V and 103° for AlSi10Mg. This behavior reflects the formation of a continuous lubricant-infused interface that effectively suppresses solid–liquid contact and minimizes adhesion.

Samples processed using picosecond laser texturing exhibited a similar wettability response. The sliding angles remained below 10°, comparable to those of SLIPS–ns surfaces, while the static contact angles were measured at approximately 105° for Ti6Al4V and 109° for AlSi10Mg. These results indicate that both laser-textured architectures support stable lubricant infusion and yield consistent low adhesion wetting behavior.

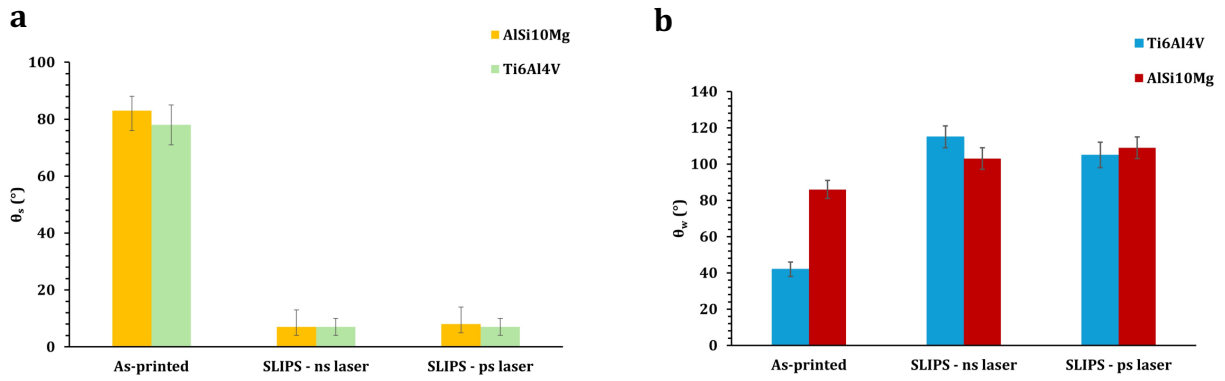

Fig. 8. Wettability of L-PBF metal samples: (a) sliding angle at different surface modification steps for AlSi10Mg and Ti6Al4V; (b) static contact angle at different surface modification steps for AlSi10Mg and Ti6Al4V.

3.3 Icing tests

Due to the significantly greater channel depth and lubricant reservoir capacity achieved using nanosecond processing, ice adhesion and cyclic anti-icing tests in this work were focused on nanosecond-processed SLIPS.

The anti-icing performance of the fabricated surfaces was evaluated by measuring ice adhesion strength using a custom shear-based test setup, schematically illustrated in Fig. 9a. A 250 µL droplet of deionized water was placed in a mold on the sample surface, frozen at −20 °C for 3 hours. After freezing, a digital force gauge was used to apply a horizontal shear force parallel to the surface until the ice detached. The maximum force (F) at detachment was recorded, and the ice adhesion strength (τ) was calculated as: $\tau = \frac{F}{A}$ where A represents the contact area between ice and substrate.

As shown in Fig. 9b, both Ti6Al4V and AlSi10Mg exhibited relatively high ice adhesion strengths in their as-printed and laser-textured states, ranging from approximately 370 to 460 kPa. These high adhesion values are attributed to the rough and porous morphology of L-PBF surfaces and the presence of native oxide layers, which promote strong mechanical interlocking and interfacial bonding with ice. Although laser texturing introduced well-defined microgrooves,

the increased surface area continued to facilitate ice anchoring, resulting in adhesion levels comparable to those of the as-printed samples.

Following SLIPS fabrication, a substantial reduction in ice adhesion strength was observed for both alloys. The adhesion strength decreased to approximately 90 kPa for AlSi10Mg and 65 kPa for Ti6Al4V, indicating the formation of a stable lubricant-infused interface that minimizes direct solid–ice contact. The infused silicone oil acts as a compliant, low-friction interlayer that suppresses interfacial bonding and facilitates ice detachment under shear loading.

The durability of the SLIPS coatings was further evaluated through four consecutive icing and de-icing cycles, as shown in Fig. 9c. For both alloys, the ice adhesion strength remained relatively stable over repeated cycles, with values consistently below 100 kPa. Minor fluctuations were observed but fell within experimental variability and are attributed to localized lubricant redistribution. Notably, Ti6Al4V exhibited slightly lower adhesion values than AlSi10Mg throughout the cycling tests, which is consistent with its more uniform and deeper laser-textured microchannel architecture that enhances lubricant confinement, as confirmed by surface topography and EDS analysis.

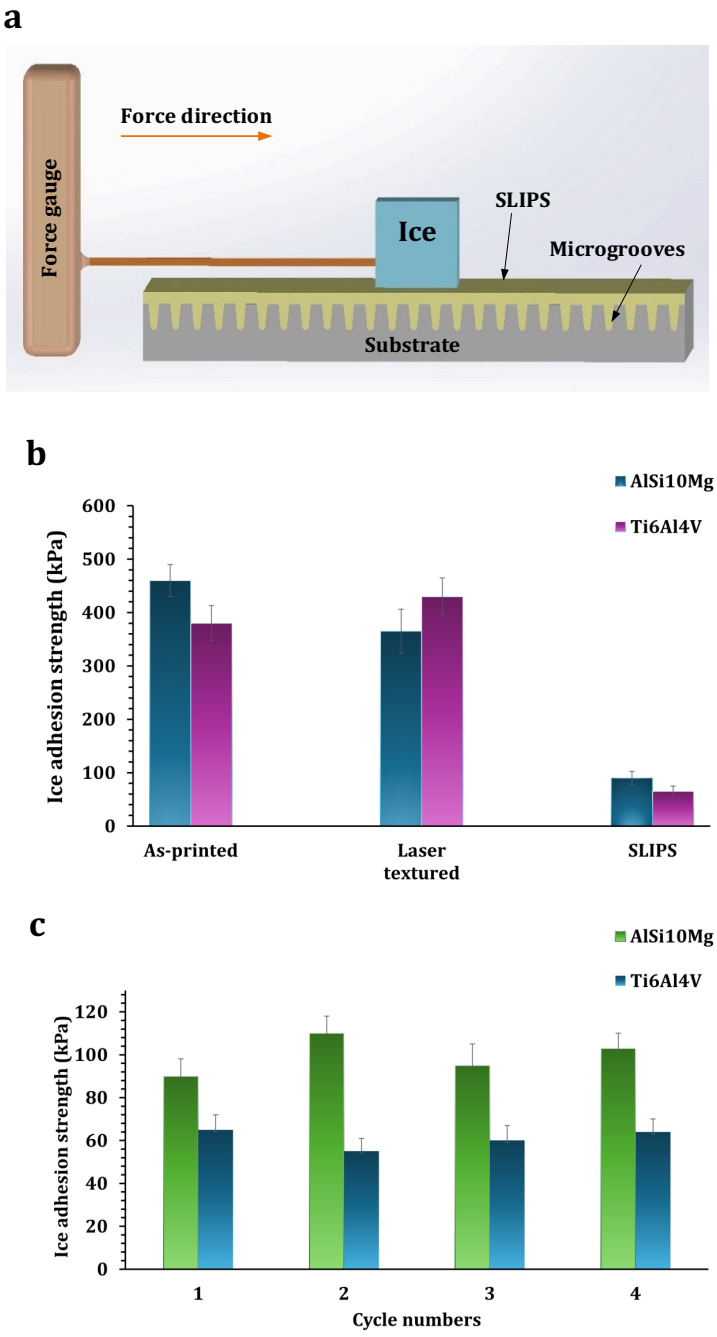

Fig. 9. Ice adhesion performance of 3D-printed Ti6Al4V and AlSi10Mg samples: (a) Schematic illustration of the shear based ice adhesion test setup; (b) Comparison of ice adhesion strength for as-printed, laser textured, and SLIPS stages; (c) Variation in ice adhesion strength of SLIPS samples over four consecutive icing and de-icing cycles.

To contextualize the performance of the SLIPS fabricated on L-PBF alloys, the present results are compared with representative studies on conventionally processed metallic substrates.

Yaghoubi et al. investigated chemically micro/nano-textured galvanized steel and reported an untreated ice adhesion strength of approximately 530 kPa, which was reduced to 12.2 kPa after silicone oil infusion [24]. Similarly, Zhang et al. demonstrated femtosecond-laser-textured aluminum, titanium, and copper surfaces, where untreated adhesion values in the range of 84–175 kPa were lowered to 5–10 kPa following lubricant infusion into laser-generated hierarchical structures [17].

More ordered porous architectures have been shown to yield even lower ice adhesion. Liu et al. reported that anodized aluminum oxide (AAO) films infused with low-viscosity silicone oil reduced ice adhesion from 398 kPa to 2.7 kPa [25]. Yuan et al. achieved comparable performance on 7075-T651 aluminum, where high-voltage anodization (110–130 V) produced a nanoporous oxide layer capable of uniform lubricant retention, lowering adhesion from 261 kPa to 6 kPa [26]. Barthwal et al. developed a micro/nano-textured 6061 aluminum surface through acid etching and anodization, followed by PDMS functionalization and silicone oil infusion, reducing adhesion from 210 kPa to 22 kPa [27]. Sattari et al. employed etching and oxidation treatments on 6061 aluminum prior to lubricant infusion, achieving a reduction in adhesion from 208 kPa to 28 kPa [28].

In comparison, the SLIPS-treated Ti6Al4V and AlSi10Mg samples developed in this work exhibit reductions in ice adhesion from approximately 380 kPa to 70 kPa and from 450 kPa to 95 kPa, respectively, corresponding to an ~80% decrease in adhesion strength. While the absolute ice adhesion values are higher than those reported for SLIPS fabricated on polished, anodized, or chemically etched substrates, the present coatings are formed directly on as-printed L-PBF surfaces with substantially higher intrinsic roughness (Sa ≈ 8–12 μm for Ti6Al4V and ≈ 20–25 μm for AlSi10Mg), representing a significantly more challenging substrate class for lubricant stabilization. Importantly, no oxide removal, anodization, or primer layers were employed, emphasizing manufacturability and process simplicity.

As summarized in Fig. 10, the normalized ice adhesion strength $\tau_n = \frac{\tau_{SLIPS}}{\tau_{untreated}}$ across all studies ranges from approximately 0.01 to 0.21, demonstrating the consistent effectiveness of silicone-oil-based SLIPS. Despite operating on inherently rough and porous additively manufactured surfaces, the L-PBF alloys investigated here achieve normalized adhesion values comparable to those reported for conventionally processed metals, underscoring the effectiveness of laser-engineered microchannel architectures for enabling durable SLIPS performance on additively manufactured components.

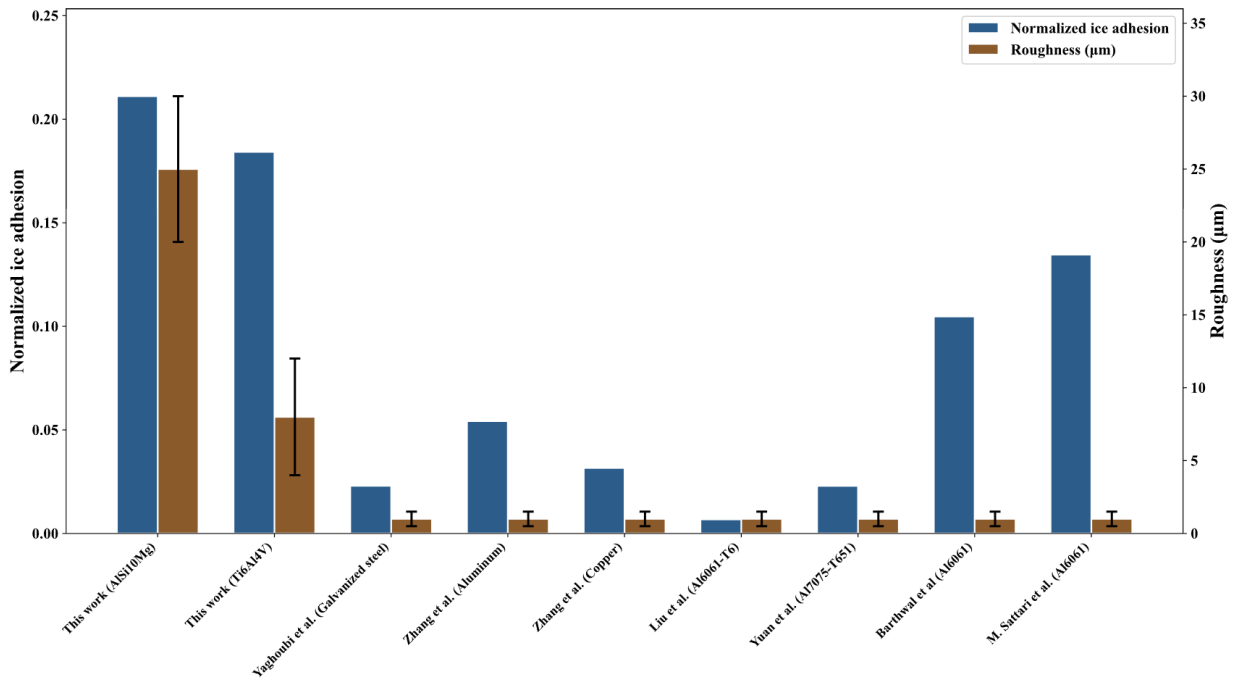

Fig. 10. Comparison of normalized ice adhesion strength and baseline substrate roughness for the present L-PBF alloys and previously reported SLIPS.

In addition, we compared the icing and deicing durability of our SLIPS coatings with several previously reported silicone oil infused surfaces to place our results in a broader context. Table 2 summarizes the reported changes in ice adhesion strength over repeated freezing cycles for different substrates and surface treatments. Although each study uses its own texturing method and surface morphology, all coatings rely on silicone oil as the infused lubricant, allowing the general durability trend to be compared across systems.

In the work of Yaghoubi et al., the micro/nano-textured galvanized steel SLIPS showed only a small increase in adhesion, rising from 12.2 kPa in the first cycle to 19.4 kPa after five cycles [24]. Barthwal et al. observed a larger change for their etched/anodized 6061 Al surface, where the adhesion increased from about 22.5 kPa to 81 kPa after fifteen cycles [27]. Liu et al., using a 10 mPa·s silicone-oil-infused AAO film, reported a very low initial adhesion which was 2.1 kPa, which increased to 23.9 kPa by the twentieth cycle due to gradual lubricant loss from the porous oxide layer [25].

Overall, both the literature data and our results show the same consistent trend which is silicone oil infused surfaces maintain low ice adhesion strength during repeated icing and deicing cycles, with the extent of the increase largely determined by how well each surface architecture retains the lubricant.

Table 2. Summary of icing and deicing durability results from this work and the literature.

Coating Description	Temp (°C)	τ_1 (kPa)	τ_{final} (kPa)	Cycles	Ref
Etched/anodized Al 6061 + silicone oil	-10	22.5	81	15	[27]
Micro/nano-textured galvanized steel + silicone oil	-10	12.2	19.4	5	[24]
AAO porous aluminum + silicone oil	-20	2.1	23.9	21	[25]
Laser-textured AlSi10Mg + silicone oil	-20	90	103	4	This work
Laser-textured Ti6Al4V + silicone oil	-20	65	64	4	This work

To further evaluate the anti-icing performance of the fabricated surfaces, the freezing behavior of water droplets on as-printed, laser-textured, and SLIPS-treated Ti6Al4V and AlSi10Mg samples was examined. A 40 µL droplet of deionized water was placed on each surface held at −15 °C, and the time required for complete solidification was recorded as the freezing delay time. Measurements were repeated 5 times per condition.

As shown in Fig. 11a, the as-printed samples exhibited the shortest freezing times, approximately 600 s for AlSi10Mg and 550 s for Ti6Al4V. These relatively rapid freezing responses are attributed to the rough, oxide-rich L-PBF surface morphology, which promotes heterogeneous ice nucleation and efficient heat transfer to the cold substrate. Laser texturing alone resulted in only a modest increase in freezing delay, yielding approximately 630 s for AlSi10Mg and 600 s for Ti6Al4V, indicating that microgrooving without lubricant infusion does not significantly suppress ice nucleation.

In contrast, SLIPS-treated samples exhibited a substantial increase in freezing delay. The freezing time increased to approximately 1200 s for AlSi10Mg and 1300 s for Ti6Al4V, representing roughly a twofold increase compared with the untreated surfaces. This improvement is attributed to the presence of a stable lubricant layer that disrupts heat transfer between the droplet and the substrate and suppresses heterogeneous nucleation by forming an intermediate, low-thermal-conductivity liquid interface [29,30].

The freezing process is visually illustrated in Fig. 11b–d for the AlSi10Mg sample. At 0 s, droplets on both untreated and SLIPS regions remain liquid. By 650 s, freezing initiates on the untreated region, while the SLIPS-coated region remains unfrozen. Complete freezing on both regions occurs by 1300 s, confirming the delayed ice formation on the SLIPS surface. The slightly longer freezing delay observed on Ti6Al4V relative to AlSi10Mg is consistent with its more uniform laser-textured microchannel architecture and improved lubricant retention, as demonstrated in the surface morphology and EDS analysis.

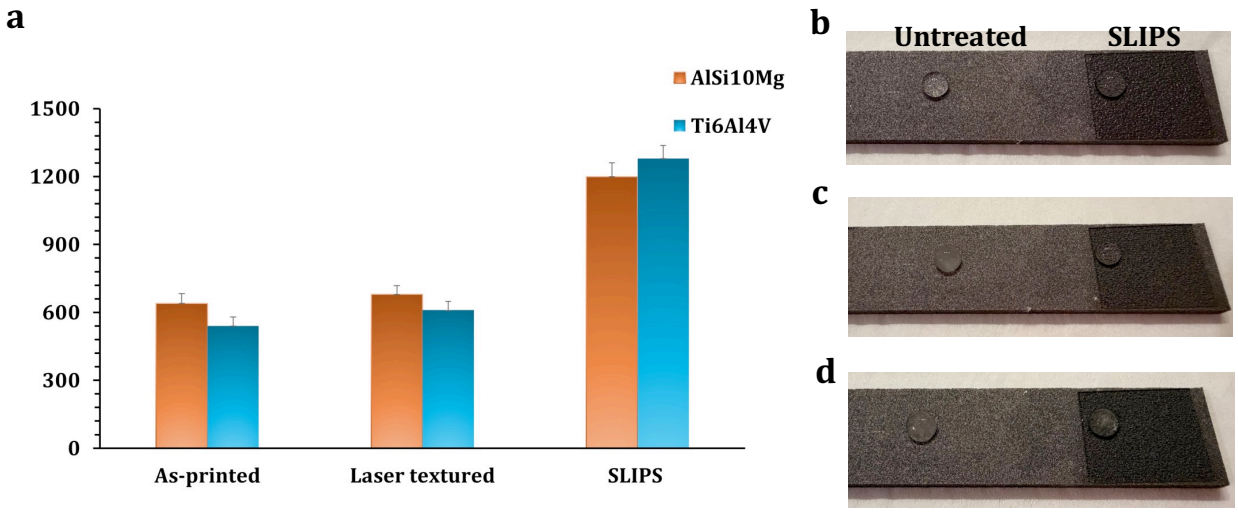

Fig. 11. Freezing behavior of water droplets on 3D-printed Ti6Al4V and AlSi10Mg surfaces at different stages at -15 °C :(a) Freezing delay times for as-printed, laser textured, and SLIPS samples. (b–d) Sequential images of droplet freezing on the AlSi10Mg surface at (b) 0 s (initial state); (c) 650 s; (d) 1300 s.

3.4 Durability of SLIPS

The mechanical durability of the SLIPS coatings was conducted on nanosecond-processed samples and evaluated using a sandpaper abrasion test. SLIPS-coated were placed face-down on 1000-grit SiC sandpaper under a 100 g normal load (Fig. 12a). One abrasion cycle consisted of one forward and one backward stroke over a length of 100 mm. After selected numbers of abrasion cycles (5, 10, 15, and 20), the ice adhesion strength was measured to assess retention of anti-icing performance.

As shown in Fig. 12b, both AlSi10Mg and Ti6Al4V samples exhibited a gradual increase in ice adhesion strength with increasing abrasion cycles. For AlSi10Mg, the adhesion strength increased from approximately 105 kPa after 5 cycles to 130 kPa after 20 cycles. Similarly, Ti6Al4V showed a smaller increase, from approximately 75 kPa to 90 kPa over the same range. Despite this increase, all values remained well below 150 kPa, indicating preserved anti-icing functionality.

The modest rise in adhesion strength is attributed to partial lubricant loss from the microchannels during repeated mechanical contact. Nevertheless, the limited degradation and stable performance over 20 cycles demonstrate the robustness and self-replenishing capability of the lubricant-infused surfaces. Notably, Ti6Al4V consistently exhibited lower adhesion values than AlSi10Mg, which is attributed to its deeper and more uniform laser-textured microchannel architecture that enhances lubricant retention.

Compared with previously reported SLIPS systems on conventionally processed aluminum alloys, which often show rapid degradation under sandpaper abrasion, the SLIPS coatings fabricated on L-PBF alloys exhibit substantially improved wear tolerance. Even after 20 abrasion cycles, both alloys maintained low ice adhesion strengths, highlighting the advantage of

combining laser-textured microchannels with additively manufactured substrates for durable SLIPS performance.

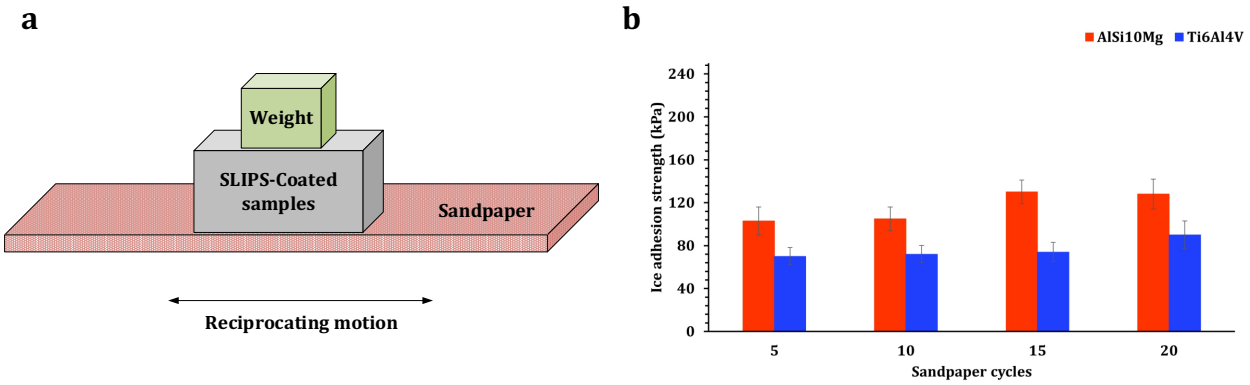

Fig. 12. Mechanical durability test: (a) Schematic of the abrasion test setup; (b) Ice adhesion strength of SLIPS-coated Ti6Al4V and AlSi10Mg after multiple sandpaper cycles.

The thermal durability of the SLIPS-coated AlSi10Mg and Ti6Al4V samples was evaluated by heating the samples in an oven to target temperatures ranging from 25 to 200 °C, with a holding time of 15 min at each temperature. After heating, the samples were allowed to cool naturally to room temperature prior to wettability characterization. The variation of the static water contact angle (θ_w) and sliding angle (θ_s) as a function of temperature is summarized in Fig. 13a.

The Ti6Al4V SLIPS surfaces exhibited excellent thermal stability over the entire temperature range. The static contact angle remained nearly constant, between approximately 115° and 120°, while the sliding angle increased only slightly from about 7° at room temperature to 11° at 200 °C. These results indicate that the silicone oil layer remained stable and uniformly distributed under thermal exposure.

In comparison, the AlSi10Mg SLIPS samples showed a greater sensitivity to heating. The static contact angle increased from approximately 103° at 25 °C to 128° at 200 °C, while the sliding angle increased more noticeably, from about 6° to 32°. Despite this increase, the surfaces retained low-adhesion behavior, confirming that the lubricant layer remained functional, albeit with reduced mobility at elevated temperatures.

The durability of the SLIPS coatings under ultraviolet (UV) exposure was further assessed by monitoring changes in the sliding angle during continuous irradiation for up to 120 min using a UV-A lamp (395 nm), as shown in Fig. 13b.. For Ti6Al4V, the sliding angle increased gradually from approximately 7° to 19°, while AlSi10Mg exhibited a similar increase from 6° to about 20°. The modest increase in sliding angle suggests limited lubricant depletion and good resistance to photochemical degradation for both alloys.

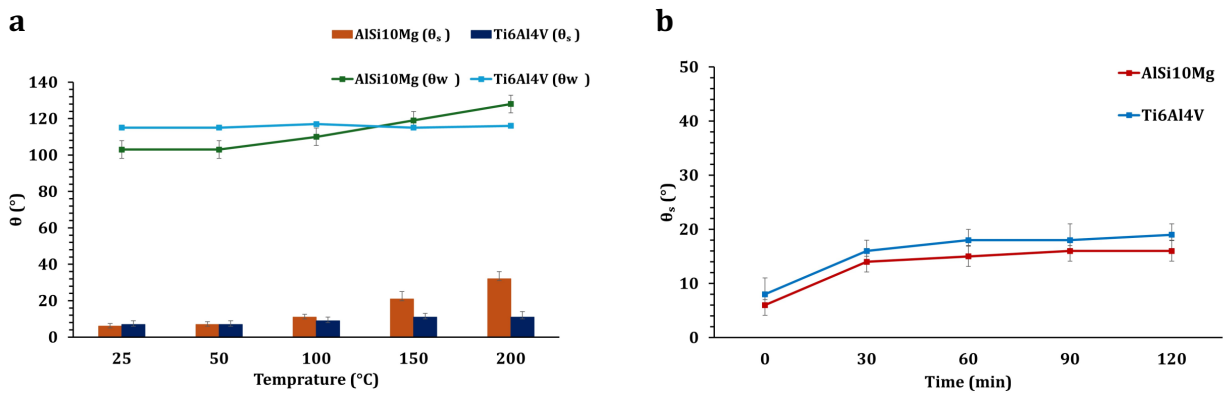

Fig. 13. Durability of SLIPS-treated Ti6Al4V and AlSi10Mg surfaces under thermal and UV exposure: (a) Variation of contact angle (θ_w) and sliding angle (θ_s) with temperature after heating each sample at defined temperatures; (b) Change in sliding angle (θ_s) during continuous UV exposure for 120 min.

4. Conclusion

In this work, we demonstrated a direct and scalable approach for fabricating SLIPS on as-printed L-PBF Ti6Al4V and AlSi10Mg alloys. By introducing laser-textured microchannel architectures onto the inherently rough AM surfaces (Sa ≈ 8–12 µm for Ti6Al4V and ≈ 20–25 µm for AlSi10Mg), stable lubricant retention was achieved despite the challenging surface topography. A comparison between nanosecond and picosecond laser texturing showed that nanosecond processing produced deeper and more continuous microchannels (~350 µm) than picosecond texturing (~20 µm), leading to improved lubricant confinement. The nanosecond-textured SLIPS reduced ice adhesion from approximately 370–460 kPa on untreated surfaces to ~65 kPa for Ti6Al4V and ~90 kPa for AlSi10Mg. The SLIPS surfaces also maintained low ice adhesion (<100 kPa) over multiple icing and deicing cycles and after up to 20 sandpaper abrasion cycles. In addition, stable wetting behavior was preserved following thermal exposure up to 200 °C and prolonged UV irradiation, with sliding angles remaining below ~20°. These results highlight an important design insight for SLIPS on additively manufactured metals: effective and durable lubricant retention requires microchannel depths that exceed the intrinsic roughness scale of the AM surface.

CRediT authorship contribution statement

Mohammad Mohammadzadeh Sanandaji: Conceptualization, Methodology, Investigation, Formal analysis, Visualization, Writing - original draft. Hao Fu: Methodology and investigation. Hongtao Ding: Conceptualization, Methodology, Resources, Supervision, Writing - review & editing, Project administration, Funding acquisition.

Declaration of Competing Interest

The authors declare that they have no known competing financial interests or personal relationships that could have appeared to influence the work reported in this paper.

Acknowledgement

The authors gratefully acknowledge the financial support from the National Science Foundation under Grant Number 2242763. We also appreciate the assistance from Prof. C. Lamuta at the University of Iowa for surface profile measurements.

Data availability

Data will be made available on request.

References

[1] Z. Liu, B. He, T. Lyu, Y. Zou, A Review on Additive Manufacturing of Titanium Alloys for Aerospace Applications: Directed Energy Deposition and Beyond Ti-6Al-4V, JOM 73 (2021) 1804–1818. https://doi.org/10.1007/s11837-021-04670-6.

[2] A. Sözen, G. Neşer, A Critical Systematic Scoping Review on the Applications of Additive Manufacturing (AM) in the Marine Industry, Polymers (Basel) 17 (2024) 4. https://doi.org/10.3390/polym17010004.

[3] M. Cheng, Y. Jiang, 3D-printed solid-state electrolytes for electrochemical energy storage devices, J Mater Res 36 (2021) 4547–4564. https://doi.org/10.1557/s43578-021-00355-7.

[4] Y. Liu, L. Ma, W. Wang, A.K. Kota, H. Hu, An experimental study on soft PDMS materials for aircraft icing mitigation, Appl Surf Sci 447 (2018) 599–609. https://doi.org/10.1016/j.apsusc.2018.04.032.

[5] A.R. Dehghani-Sanij, S.R. Dehghani, G.F. Naterer, Y.S. Muzychka, Sea spray icing phenomena on marine vessels and offshore structures: Review and formulation, Ocean Engineering 132 (2017) 25–39. https://doi.org/10.1016/j.oceaneng.2017.01.016.

[6] M. Farzaneh, W.A. Chisholm, Techniques for Protecting Overhead Lines in Winter Conditions, Springer International Publishing, Cham, 2022. https://doi.org/10.1007/978-3-030-87455-1.

[7] L. Battisti, Wind Turbines in Cold Climates, Springer International Publishing, Cham, 2015. https://doi.org/10.1007/978-3-319-05191-8.

[8] R. Fürstner, W. Barthlott, C. Neinhuis, P. Walzel, Wetting and self-cleaning properties of artificial superhydrophobic surfaces, Langmuir 21 (2005) 956–961. https://doi.org/10.1021/la0401011.

[9] J. Yong, Q. Yang, C. Guo, F. Chen, X. Hou, A review of femtosecond laser-structured superhydrophobic or underwater superoleophobic porous surfaces/materials for efficient oil/water separation, RSC Adv 9 (2019) 12470–12495. https://doi.org/10.1039/c8ra10673h.

[10] J.C. Bird, R. Dhiman, H.M. Kwon, K.K. Varanasi, Reducing the contact time of a bouncing drop, Nature 503 (2013) 385–388. https://doi.org/10.1038/nature12740.

[11] W. Huang, B. Nelson, S. Tian, R. Ordikhani-Seyedlar, R.C.Y. Auyeung, A. Samanta, H. Hu, S. Shaw, C. Lamuta, H. Ding, Superhydrophobic surface processing for metal 3D printed parts, Appl Mater Today 29 (2022). https://doi.org/10.1016/j.apmt.2022.101630.

[12] D. Tripathi, P. Ray, A.V. Singh, V. Kishore, S.L. Singh, Durability of Slippery Liquid-Infused Surfaces: Challenges and Advances, Coatings 13 (2023). https://doi.org/10.3390/coatings13061095.

[13] T. Verho, J.T. Korhonen, L. Sainiemi, V. Jokinen, C. Bower, K. Franze, S. Franssila, P. Andrew, O. Ikkala, R.H.A. Ras, Reversible switching between superhydrophobic states on a hierarchically structured surface, Proceedings of the National Academy of Sciences 109 (2012) 10210–10213. https://doi.org/10.1073/pnas.1204328109.

[14] T.S. Wong, S.H. Kang, S.K.Y. Tang, E.J. Smythe, B.D. Hatton, A. Grinthal, J. Aizenberg, Bioinspired self-repairing slippery surfaces with pressure-stable omniphobicity, Nature 477 (2011) 443–447. https://doi.org/10.1038/nature10447.

[15] P. Kim, T.S. Wong, J. Alvarenga, M.J. Kreder, W.E. Adorno-Martinez, J. Aizenberg, Liquid-infused nanostructured surfaces with extreme anti-ice and anti-frost performance, ACS Nano 6 (2012) 6569–6577. https://doi.org/10.1021/nn302310q.

[16] S. Anand, A.T. Paxson, R. Dhiman, J.D. Smith, K.K. Varanasi, Enhanced condensation on lubricant-impregnated nanotextured surfaces, ACS Nano 6 (2012) 10122–10129. https://doi.org/10.1021/nn303867y.

[17] J. Zhang, Q. Yang, Y. Cheng, Z. Fang, X. Hou, F. Chen, Slippery Liquid-Infused Porous Surface on Metal Material with Excellent Ice Resistance Fabricated by Femtosecond Bessel Laser, Adv Eng Mater 24 (2022). https://doi.org/10.1002/adem.202101738.

[18] K. Sakuraba, S. Kitano, D. Kowalski, Y. Aoki, H. Habazaki, Slippery Liquid-Infused Porous Surfaces on Aluminum for Corrosion Protection with Improved Self-Healing Ability, ACS Appl Mater Interfaces 13 (2021) 45089–45096. https://doi.org/10.1021/acsami.1c13071.

[19] R. Deng, T. Shen, H. Chen, J. Lu, H.C. Yang, W. Li, Slippery liquid-infused porous surfaces (SLIPSs): A perfect solution to both marine fouling and corrosion?, J Mater Chem A Mater 8 (2020) 7536–7547. https://doi.org/10.1039/d0ta02000a.

[20] B. Nelson, W. Huang, H. Ding, An analysis of surface texture and wetting behavior for metal alloys produced by laser-powder bed fusion, Manuf Lett 35 (2023) 540–548. https://doi.org/10.1016/j.mfglet.2023.08.020.

[21] A. Samanta, W. Huang, H. Chaudhry, Q. Wang, S.K. Shaw, H. Ding, Design of Chemical Surface Treatment for Laser-Textured Metal Alloys to Achieve Extreme Wetting Behavior, ACS Appl Mater Interfaces 12 (2020) 18032–18045. https://doi.org/10.1021/acsami.9b21438.

[22] M. Mohammadzadeh Sanandaji, R. Mollick, A. Ratner, H. Ding, Laser-enabled organic coating for sustainable PFAS-free metal surfaces, Manuf Lett 45 (2025) 8–12. https://doi.org/10.1016/j.mfglet.2025.06.198.

[23] A. Samanta, Q. Wang, S.K. Shaw, H. Ding, Roles of chemistry modification for laser textured metal alloys to achieve extreme surface wetting behaviors, Mater Des 192 (2020). https://doi.org/10.1016/j.matdes.2020.108744.

[24] M. Yaghoubi, N. Parvini Ahmadi, S. Yazdani, Fabrication of slippery lubricant-infused porous surfaces of galvanized steel with durable anti-icing and anti-corrosion behavior, Mater Today Commun 42 (2025). https://doi.org/10.1016/j.mtcomm.2024.111251.

[25] G. Liu, Y. Yuan, R. Liao, L. Wang, X. Gao, Fabrication of a porous slippery icephobic surface and effect of lubricant viscosity on anti-icing properties and durability, Coatings 10 (2020). https://doi.org/10.3390/COATINGS10090896.

[26] Y. Yuan, L. Wang, G. Liu, R. Liao, Fabrication of ultralow ice-adhesion slippery liquid infused porous surfaces on aluminum alloy (7075-t651), Coatings 10 (2020) 1–11. https://doi.org/10.3390/coatings10111025.

[27] S. Barthwal, B. Lee, S.H. Lim, Fabrication of robust and durable slippery anti-icing coating on textured superhydrophobic aluminum surfaces with infused silicone oil, Appl Surf Sci 496 (2019). https://doi.org/10.1016/j.apsusc.2019.143677.

[28] M. Sattari, A. Olad, F. Maryami, I. Ahadzadeh, K. Nofouzi, Facile fabrication of durable and fluorine-free liquid infused surfaces on aluminum substrates with excellent anti-icing, anticorrosion, and antibiofouling properties, Surfaces and Interfaces 38 (2023). https://doi.org/10.1016/j.surfin.2023.102860.

[29] J. Lee, M.H. Lee, C.H. Choi, Design of Robust Lubricant-Infused Surfaces for Anti-Corrosion, ACS Appl Mater Interfaces 14 (2022) 2411–2423. https://doi.org/10.1021/acsami.1c22587.

[30] P. Zhang, Z. Guo, Robust anti-icing slippery liquid-infused porous surfaces inspired by nature: A review, Materials Today Physics 46 (2024) 101478. https://doi.org/10.1016/j.mtphys.2024.101478.